Substitution of Titanium for Magnesium Ions at the Surface of Mg-Doped Rutile

Céline Dupont, Jacques Jupille, Sylvie Bourgeois, Patrick Le Fèvre, Alberto Verdini, Luca Floreano, Bruno Domenichini

Substitution of titanium for magnesium ions at the surface of rutile

Celine Dupont,[*,†] Jacques Jupille,[‡] Sylvie Bourgeois,[†] Patrick Le Fèvre,[¶] Alberto Verdini,[§] Luca Floreano,[§] and Bruno Domenichini[†]

Laboratoire Interdisciplinaire Carnot de Bourgogne (ICB), UMR 6303 CNRS, Université Bourgogne Franche-Comté, BP 47870, 21078 Dijon Cedex, France, Institut des NanoSciences de Paris, Sorbonne University and CNRS, Campus de Jussieu, F-75252 Paris, France, Synchrotron SOLEIL, L'Orme des Merisiers, BP 48, 91192 Gif-sur-Yvette, France, and Instituto Officina dei Materiali IOM-CNR, Laboratorio TASC s.s. 14 km 163.5, 34149 Trieste, Italy

E-mail: celine.dupont@u-bourgogne.fr

Abstract

The surface structure of Mg-doped rutile TiO_2(011) surfaces is determined by combining core level/valence band photoemission and photoelectron diffraction (PED) to evolutionary algorithm, density functional theory (DFT) and multiple scattering calculations. Upon annealing the reduced crystal above 620 K, Mg segregates by substitution to Ti atoms from the TiO_2 lattice while keeping the known reconstruction of the Mg-free surface. Band gap states being totally healed by Mg segregation, the charge compensation is provided by O vacancies as formally expressed by the Kröger and Vink notation. A full support to those findings comes from

[*]To whom correspondence should be addressed

[†]Laboratoire Interdisciplinaire Carnot de Bourgogne (ICB), UMR 6303 CNRS, Université Bourgogne Franche-Comté, BP 47870, 21078 Dijon Cedex, France

[‡]Institut des NanoSciences de Paris, Sorbonne University and CNRS, Campus de Jussieu, F-75252 Paris, France

[¶]Synchrotron SOLEIL, L'Orme des Merisiers, BP 48, 91192 Gif-sur-Yvette, France

[§]Instituto Officina dei Materiali IOM-CNR, Laboratorio TASC s.s. 14 km 163.5, 34149 Trieste, Italy

DFT calculations based on findings from evolutionary algorithm calculations which demonstrate that a combination of four surface structures nicely accounts for the observed experimental Ti 3s and Mg 2s patterns. These model structures only involve Mg in substitutional position and O vacancies, whereas neither interstitial atoms nor excess electrons are experimentally detected.

Introduction

Doping titanium dioxide by aliovalent cations is an actively pursued route to tailor the multiple properties of this material[1]. Depending on how the cation valence structure compares with that of titanium (either donor or acceptor), the doping elements modify the gap width[2], change the electrical conductivity and shift the flat band potential[3]. In this context, the numerous applications of Al- and Mg-doped TiO_2 have attracted much attention. Aluminum-doping reduces the photocatalytic activity of TiO_2 pigments by widening the band gap and trapping the photogenerated charges[4]. Both Mg-[5–9] or Al-doped[10] TiO_2 improve the performances of dye-sensitised solar cells through the increase of the open circuit voltage[10]. Similarly, Mg-doped TiO_2 electron transport layers improve the efficiency of perovskite solar cells[11]. The reversible intercalation of multivalent Mg^{2+} and Al^{3+} ions in anatase with a high concentration of cation (Ti) vacancies was brought forward as a proof of concept for increasing the volumetric energy densities in multivalent batteries[12]. Finally, Mg-doped titanium dioxide is frequently used to promote photocatalytic reactions such as photoreduction of CO_2[13], oxidation of NO[14] and photodegradation[15,16].

The Al and Mg insertion modes are quite similar. Both elements are suggested to occupy substitutional sites accompanied by oxygen vacancies for charge compensation, hence preserving the initial structure of the oxide[6,10,12,15,17,18]. The substitution of Ti ions by Mg[6,12,15] and Al[10,17,18] ions in the TiO_2 lattice is favored by the similarity of the ionic radius of Al^{3+} (0.53 Å) and Mg^{2+} (0.72 Å) with that of Ti^{4+} (0.68 Å)[19]. Regarding electronic properties, pristine titanium dioxide can be easily reduced to a n-type semiconductor through the formation of both oxygen vacancies

and titanium interstitials ions[20]. Those two types of intrinsic point defects generate excess electrons that populate the Ti 3d band gap states (BGS)[21] located within the band gap at about 0.8 eV below the Fermi level as observed experimentally[22–26] and modeled by hybrid DFT calculations[27]. Substitution of Ti atoms by Al atoms is predicted to heal the band gap states[10,17,18]. Owing to the importance of the topic, a variety of techniques focused on the impact of doping on the crystallographic and electronic structure of the oxide, including x-ray absorption[28], x-ray scattering[12], electron paramagnetic resonance[28,29] and nuclear magnetic resonance[12]. However, despite intensive efforts, the still vivid debate on the actual doping element/vacancy ratio and on the occurrence of interstitial positions for doping elements[10,17,18,30] remains central in the understanding of the crystallography of doped oxides, the subject being further complicated by the sensitivity of the actual properties of doped TiO_2 to synthesis conditions[8,10,12].

Quite efficient for investigating bulk properties, the aforementioned methods are hardly relevant to analyze the extreme surface of the solids which plays an important role in many applications. For example, surface structure is a key parameter in catalysis and photocatalysis and in dye-sensitized and perovskite solar cells in which it drives charge transfer. The present work takes up the challenge of the analysis of the surface defect states of Mg-doped TiO_2(011) rutile. Besides, whereas the bulk structure of Al-doped TiO_2 has been abundantly studied[10,17,18], the Mg-doped one has never been investigated. We combine herein experimental data - surface sensitive core level and valence band photoemission and resonant photoelectron diffraction (PED) experiments - with a theoretical analysis based on evolutionary algorithm, density functional theory (DFT) and multiple scattering calculations. Resonant PED experiments supported by calculations have proven to be an extremely relevant tool to determine the structure of the rutile (110)[31,32] and (011)[33] surface regions. The technique shows a great sensitivity to small defects concentrations, thanks to the enhancement of the Ti 3d emission through the resonant valence-band photoemission process[31,32]. At the Ti $L_{2,3}$ edge, the direct photoemission from the valence-band states (with the Ti 3d character) overlaps and interferes with the Auger-like autoionization process, in particular

with the participator decay channel that leads to the same final state of a VB photoemission[34–36]. Of particular interest in the case under study, PED could demonstrate that the defective Ti 3d sites mostly lie on the subsurface layers of the rutile TiO_2(110) surface[31,32], a result latter supported by an electron energy loss study of the origin and depth profile of band gap states (BGS)[21]. Such an ability to probe the existence and localization of excess electrons is central in the present work which aims to examine (i) the surface structure of a Mg-doped rutile TiO_2(011) crystal, (ii) the mode of insertion of Mg atoms and (iii) the behavior of the excess electrons in the presence of the doping element.

Methods

Experimental

The experiments were performed at the ALOISA beamline[37] of the Elettra Synchrotron Light Source in Trieste, Italy, in an ultra-high vacuum chamber (base pressure 10^{-10} mbar) that has already been described[31,37]. We used a TiO_2(011) crystal (SurfaceNet GmbH) doped by magnesium that could easily segregate by annealing. This single sample, which contains magnesium as random impurity, offers the opportunity to explore the surface structure of a doped oxide. The amount of magnesium is below the detection limit of this element by electron microprobe analysis (ca. 1%). It was carefully checked by photoemission that no other impurity appeared during the experiments. The sample was prepared under vacuum through cycles of argon ion bombardment (1 keV, 30 min) followed by annealing at different temperatures. For photoemission and PED experiments, the X-ray beam was impinging the sample at grazing incidence (4°) with light polarization normal to the surface. Surface analysis was performed by photoemission from the Mg 2p and Ti 3p levels at a primary photon energy of 140 eV. This energy allows (i) a relatively larger sensitivity to Mg rather than to Ti, thanks to the favorable photoionization cross section of Mg 2p (3.4 Mbarn) compared to that of Ti 3p (1.2 Mbarn)[38] and (ii) the best surface sensitivity due to an electron escape depth

as short as ∼5 Å for both Mg 2p and Ti 3p photoelectrons. Instead, to study the valence band in conditions allowing the resonant enhancement of the Ti 3d defect states, the chosen photon energy was 462.5 eV. It corresponds to the Ti L_2 threshold, as determined by XANES measurements[35]. We performed PED measurements on the Mg-doped rutile crystal by recording the Mg 2s and Ti 3s core levels intensities as a function of polar and azimuthal angles. Even if the cross sections of these levels are smaller than those of the corresponding p levels, experimental values of the peak area are easier to extract since the quantitative analysis of the area of the Mg 2p spectral line requires to subtract the Ti 3p shake up satellite that is superposed to it (see Figure 1). The kinetic energies for the PED experiments were 428 eV and 455 eV, for the Mg 2s and the Ti 3s lines, respectively. All measurements were done at room temperature.

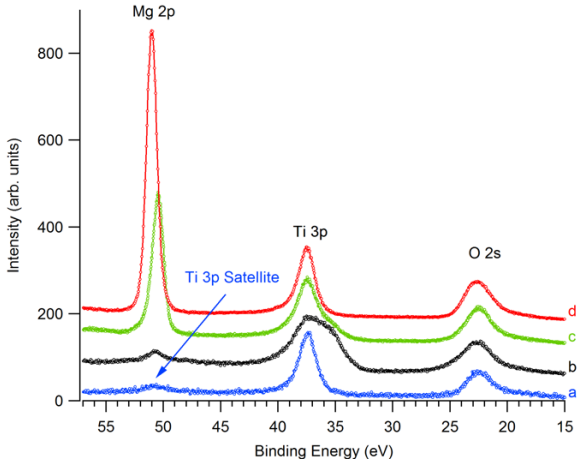

Figure 1: Photoemission spectra recorded at a photon energy of 140 eV over the binding energy range corresponding to the Mg 2p, Ti 3p and O 2s core levels, for surfaces of different rutile TiO_2(011) samples: (a) Mg-free crystal sputtered and annealed at 870 K; (b) Mg-doped crystal after sputtering; (c) same as (b) after annealing at 620 K for 3 minutes; (d) same as (b) annealed at 870 K for 3 minutes.

PED patterns were recorded by scanning the azimuthal angle ϕ over 110° including both symmetry directions $[01\bar{1}]$ and $[00\bar{1}]$. The polar angle θ was varied from -2 to 80°, where 0° corresponds to the direction normal to the surface. The step size was 2° for both ϕ and θ. In order to obtain the full ϕ range of 360°, the measured patterns were folded symmetrically according to the C2v point symmetry of the surface. The symmetry was checked for Ti 2p PED with a few wider ϕ

scans. The PED patterns are reported as χ functions with:

$$\chi(\theta,\phi) = \frac{I(\theta,\phi) - I_0(\theta)}{I_0(\theta)} \tag{1}$$

where $I_0(\theta)$ is given by the ϕ-average of the photoemission intensity $I(\theta,\phi)$ measured at polar angle θ and azimuth ϕ and represents the non-diffractive contribution[39].

To analyse the difference between two patterns χ_A and χ_B, we used the structure reliability factor, R_f, defined as:

$$R_f = \sum(\chi_A - \chi_B)^2 / \sum(\chi_A^2 + \chi_B^2) \tag{2}$$

where the sum is performed over the whole experimental angular ranges. $R_f = 0$ and $R_f = 1$ correspond to identical and uncorrelated datasets, respectively.

Computational details

DFT calculations have been used to model and optimize the structure of Mg-doped rutile, before the PED modeling. However, considering the numerous possibilities for Mg doping in the TiO_2(011) crystal, a comprehensive human screening appears as a huge and waste of time undertaking. Starting with compositions deduced from XPS experiments, we used the evolutionary algorithm implemented in USPEX[40–43] in combination with total energy DFT calculations through the VASP code[44,45] to determine the structure of doped rutile. Evolutionary algorithm calculations were performed through fixed compositions calculations using the surface method implemented in USPEX, with the system divided in substrate, buffer and surface regions. In agreement with experimental results, Mg atoms were included only in the surface region. Seeds structures derived from the rutile TiO_2(011) reconstruction previously published[33] were also included.

The most stable structures given by USPEX were then optimized at higher accuracy with VASP, following the conditions we already published[33]. In particular the system was modeled by symmetric slabs of 11 layers, with reconstruction and Mg on both sides. Total energy calculations were performed at the GGA+U level with the PBE[46] functional and U_{eff} = 4.2 eV in the Du-

darev's approach[47]. The projector augmented-wave (PAW) method has been used, with twelve valence electrons for Ti (namely, $3s^2$ $3p^6$ $4s^2$ and $3d^2$), six for O (namely, $2s^2$ and $2p^4$), and two for Mg (namely, $3s^2$ and $3p^0$) and a converged plane-wave cutoff of 500 eV has been applied. A $3\times3\times1$ Monkhorst-Pack[48] k-point mesh was used to sample the first Brillouin zone. The geometry optimization was completed when forces were smaller than 0.01 $eV.^{-1}$. PED patterns of the best candidates, namely the most stable, were then modeled by performing multiple scattering calculations using the EDAC code[49], within the cluster approach.

Results and Discussion

Reoxidation of the rutile surface

Photoemission spectra involving the Mg 2p, Ti 3p and O 2s core levels and the corresponding valence band region are shown in Figures 1 and 2, respectively. Spectra recorded on the Mg-free TiO_2(011) crystal prepared in similar conditions as the Mg-doped rutile sample are shown in both figures for comparison (bottom (a) curves). Upon sputtering the Mg-doped TiO_2(011) crystal, a Mg-free surface is obtained confirming the very low concentration of Mg in the material. The strong component seen on the lower binding energy side of the Ti 3p line stems from the reduced Ti atoms whose formation goes with the appearance of oxygen vacancies (Figure 1(b)). Mg segregates after a mild annealing at 620 K for 3 minutes (Figure 1(c)). Subsequent annealing at temperatures higher than 870 K for 3 minutes (Figure 1(d)) leads to additional Mg segregation. Owing to the proximity of the binding energies of the two levels, escape depths were judged similar. The Ti 3p binding energy of 37.4 eV is similar to that of stoichiometric TiO_2. The binding energy of Mg 2p is 50.5 eV for the annealing at 620 K and 50.9 eV for the magnesium richest surface obtained after annealing at 870 K. Both values are close to that found for oxidized Mg[50]. The shifted Ti 3p component, which is associated with a reduction of the oxide, decreases in intensity upon annealing at 620 K (Figure 1(c)). It is no longer observed after annealing at 870 K (Figure 1(d)).

Spectra of the valence band region are shown in Figure 2 at the excitation energy of the Ti L_2

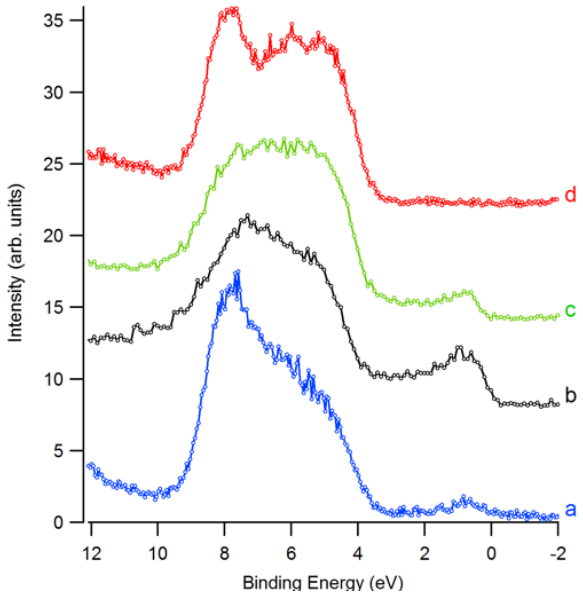

Figure 2: Spectra of the valence band region on the same rutile TiO_2(011) surfaces as in Figure 1. Spectra are recorded at 462.5 eV *i.e.* at Ti 2p $\rightarrow$ Ti 3d threshold in order to enhance the band gap state (see text).

edge (on-resonance) for higher sensitivity to the band gap state (BGS). As a result of argon ion sputtering the TiO_2(011) surface, a Ti 3d BGS appears at a binding energy of $\sim$0.8 eV (Figure 2(b)), as commonly observed in photoemission spectra of defective rutile surfaces[22–25]. The BGS (Figure 2(b)) and the Ti 3p lower binding energy shift[51] are both fingerprints of the reduction of the oxide which is formally expressed by $Ti^{4+} \rightarrow Ti^{n+}$ with $n < 4$. Upon annealing the ion-bombarded Mg-doped sample, Mg segregates within the surface layers (Figures 1(c) and (d)). In addition, the feature associated with the Ti 3d states in the valence spectra decreases (Figures 2(c) and (d)). It even totally disappears at 870 K for the Mg richest surface. In this case, the Ti 3d level is totally empty which means that, in the layers probed by the photoemission analysis, the Ti atoms have been fully reoxidized and are only in the Ti^{4+} oxidation state. Finally, it should be noticed that in the case of pristine rutile, the reoxidation of the reduced surface via the inward diffusion of interstitial titanium ions occurs rapidly above 740 K[52]. Therefore, the fast healing of the BGS observed at a temperature as low as 620 K at the surface of the Mg-doped TiO_2 is likely associated to the surface segregation of Mg.

Localization of magnesium atoms

Determining the position of Mg atoms in the structure consists in refining, at the atomic scale, the structure of the topmost layers by combining experimental results and multiple scattering simulations with a theoretical approach based on DFT calculations, as we already did for determining the reconstruction of undoped $TiO_2(011)$[33]. Many parameters have to be taken in account: proportion of Ti atoms substituted by Mg atoms, distribution and positions of these Mg atoms in the surface layers, distribution of oxygen vacancies (O_{vac}) related to the presence of Mg atoms as well as structural relaxations due to substituted cations and O_{vac}. As it is impossible to carry out an exhaustive study of all cases, some assumptions must be made. The choice of the refined structure will be guided by the quantitative analysis of the experimental data and the energy of the calculated structures, as determined by DFT.

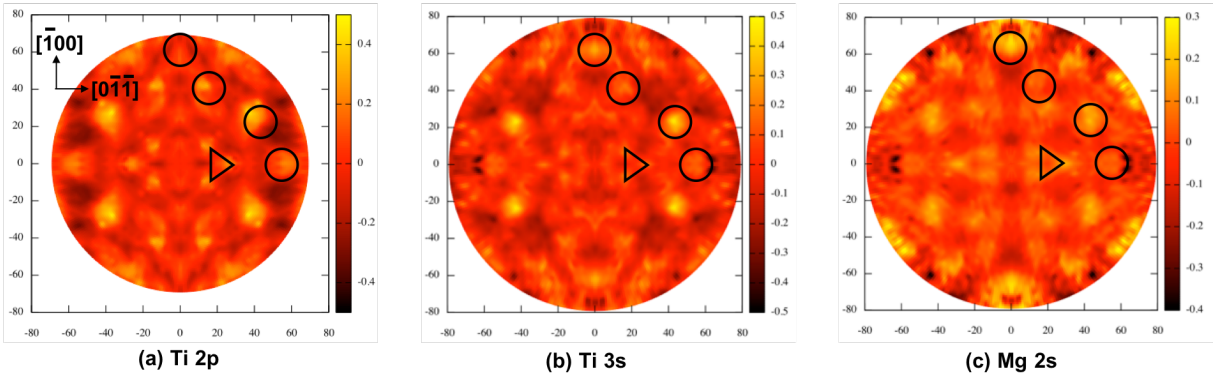

Figure 3: PED patterns of (a) the Ti 2p level of the Mg-free $TiO_2(011)$ crystal[33] measured at a kinetic energy of 464 eV, (b) the Ti 3s and (c) the Mg 2s levels of the Mg-doped crystal after annealing to 870 K, measured at kinetic energies of 455 and 428 eV, respectively. The projection is linear, with the polar angle $\theta = 0\ ^\circ$ along the surface normal. The azimuth $\phi = 0\ ^\circ$ is found at 3 o'clock along <$\bar{1}$00> and $\phi = 90\ ^\circ$ is found at 12 o'clock along <0$\bar{1}\bar{1}$>. The main well-defined spots of the Ti 3s pattern have been surrounded by circles and triangles which were then applied without change on the Ti 2p and Mg 2s patterns. (Ti 3s was taken as reference because it can be compared to both the Mg 2s pattern recorded on the same doped crystal and to the Ti 2p pattern from the Mg-free crystal.)

We start the analysis by comparing the Ti 2p PED pattern measured on the Mg-free $TiO_2(011)$ crystal (Figure 3(a)) with the PED patterns measured on the Mg-doped sample at the Ti 3s (see Figure 3(b)) and Mg 2s (Figure 3(c)) levels. A simple visual inspection reveals that the three ex-

perimental patterns share many features. We highlighted the main features of the Ti 3s pattern on the Mg-doped crystal by drawing a set of circles and triangles (Figure 3(b)). The same set of markers is rigidly superimposed to the Ti 2p and Mg 2s PED patterns of the undoped and Mg-doped crystals, respectively. From the strong similarity of the main diffraction features (in terms of intensity and angular position), one can infer (i) that the lattice structure of Ti in the topmost layers is practically unaffected by the Mg atoms and (ii) that Mg atoms are mostly present in the TiO_2 topmost layers as substitutional ions. In particular, the characteristic reconstruction of the Mg-free $TiO_2(011)$ surface[33], which gives rise to the three spots at the vertex of the triangles, is preserved in the Mg-doped crystal. Therefore, we may assume the reconstruction of the Mg-free $TiO_2(011)$ surface[33] as a reference starting model for further refinement of the Mg-doped surface. Additionally, the anisotropy scales (Figures 3(b) and (c)) indicate that the amplitude of the anisotropy χ of Mg 2s is about half that of Ti 3s. The observation suggests that Mg atoms may sit in a less ordered local environment than the Ti atoms or in a part of the material where the diffraction contribution originated by forward scattering is weaker, which points to the very topmost layers. We may thus assume that Mg atoms are distributed over a few cationic layers only, allegedly a maximum of three.

In order to estimate the amount of Mg atoms distributed in the upper layers, we first considered a quantitative study of the photoemission spectra at 140 and 462.5 eV. A simple analysis of the ratio Mg 2s/Ti 3s from the intensities of the components determined by photoemission does not allow the determination of the exact number of Mg atoms substituting Ti. Indeed, an atom in the topmost layer yields a larger photoemission contribution than an atom of deeper layers. In other words, a single experimental ratio Mg 2s/Ti 3s can be modeled in multiple different ways. If we assume that Mg atoms are mostly distributed in the three topmost cationic layers, as suggested by the amplitude of the PED anisotropy, several distributions (Table 1) might be derived from the measured experimental ratios on the basis of the tabulated photoionization sections and of the inelastic mean free paths (IMFP) of the electrons – taken identical for Mg 2s and Ti 3s insofar as their kinetic energy differs by only a few percent. This approach allows us to determine that between eight

and twelve magnesium atoms are spread over the two or three first layers. To confirm this result, similar simulations have been done for the Mg 2p/Ti 3p ratio measured for a much lower exciting photon energy (140 eV), thus yielding an analysis much more sensitive to the surface. Here again, distributions with a rate of Mg between eight and twelve atoms are obtained (Table 1).

Table 1: Mg/Ti ratios calculated as a function of the number of Mg atoms spread over the two or three first layers. Mg 2p and Ti 3p are analyzed with a 140 eV photon source and Mg 2s and Ti 3s with photon energy of 462.5 eV. Possible configurations - those with a deviation below 25% - are highlighted.

	Mg/Ti ratio			
	Mg 2p/Ti 3p = 3.11		Mg 2s/Ti 3s = 0.66	
number of Mg spread on ...	... 3 planes [22 Ti sites]	... 2 planes [14 Ti sites]	... 3 planes [22 Ti sites]	... 2 planes [14 Ti sites]
1	0.16	0.21	0.04	0.05
2	0.34	0.44	0.09	0.11
3	0.54	0.71	0.14	0.17
4	0.76	1.01	0.19	0.23
5	1.00	1.35	0.25	0.30
6	1.26	1.74	0.31	0.37
7	1.55	2.19	0.37	0.45
8	1.89	2.73	0.44	0.54
9	2.26	3.38	0.51	0.63
10	2.69	4.16	0.59	0.73
11	3.20	5.15	0.68	0.85
12	3.76	6.40	0.77	0.97
13	4.43	7.38	0.87	1.07

Following results of Table 1, we have performed different USPEX calculations for the five concentrations of Mg, spread over the three upper layers. The most stable structure presents a surface energy of 76 meV/Å^2 with a Mg concentration of nine atoms spread over the two topmost layers of the simulation cell. Considering that the thermal energy is approximatively 20 meV at room temperature, our operating condition, all structures presenting a surface energy lower than 100 meV/Å^2 are considered as realistic. This criterium discards all structures with ten or more magnesium atoms. Thus there remain only fifteen structures presenting a surface energy below 100 meV/Å^2 with either eight or nine Mg atoms.

For this final set of energy favored configurations, we calculated the PED patterns and we evaluated

the corresponding structural reliability factor (R_f). We first considered the Ti 3s PED diagram to discriminate among the possible configurations. The final R_f is optimized by considering all possible combinations of the fifteen structures. With this last refinement, only the four structures reported in Figure 4 are retained to appear in the final description. Hence a single model cannot be drawn for Mg-doped TiO_2(001), but rather a family of four configurations, each one with eight Mg atoms spread over the two first layers, whereas all structures with nine Mg atoms have been discarded because they do not yield any optimization of the overall R_f(Ti 3s). This combination of structures, weighted as reported in Table 2, leads to R_f(Ti 3s) = 0.69 and R_f(Mg 2s) = 0.61. According to the DFT models, these structural configurations involve six Ti atoms and eight Mg atoms in substitutional positions over the first two layers. With respect to the defect-free rutile structure, it corresponds to twenty O atoms or, in other word, to eight O_{vac} corresponding to a percentage of 29%.

Table 2: Surface energy (in meV/Å^2), R_f for Ti 3s, R_f for Mg 2s and contribution (in %, with an uncertainty of $\pm$1%) in the final structure of the four retained configurations. Averaged values are given for the final configuration.

	E(meV/Å^2)	R_f(Ti 3s)	R_f(Mg 2s)	Contribution (%)
Structure (a)	89	0.71	0.66	50
Structure (b)	95	0.77	0.81	20
Structure (c)	97	0.74	0.56	15
Structure (d)	98	0.74	0.78	15
Combination	93	0.69	0.61	

The simulated PED patterns of the Ti 3s and Mg 2s levels obtained with the optimal combination defined in Table 2 are reported in Figure 5 together with the experimental patterns, as taken from Figure 3. Sets of circles, ovals and triangles are used to highlight the main features of the experimental patterns. For both atomic species, the position of spots on the simulated patterns almost perfectly reproduce the experimental features. The disagreements mostly come from missing spots, like that marked with a blue cross in the case of Mg 2s. This means that the selected structures (Figure 4) fairly represent the actual positions of Ti and Mg atoms and only few Mg atoms escape our structural analysis.

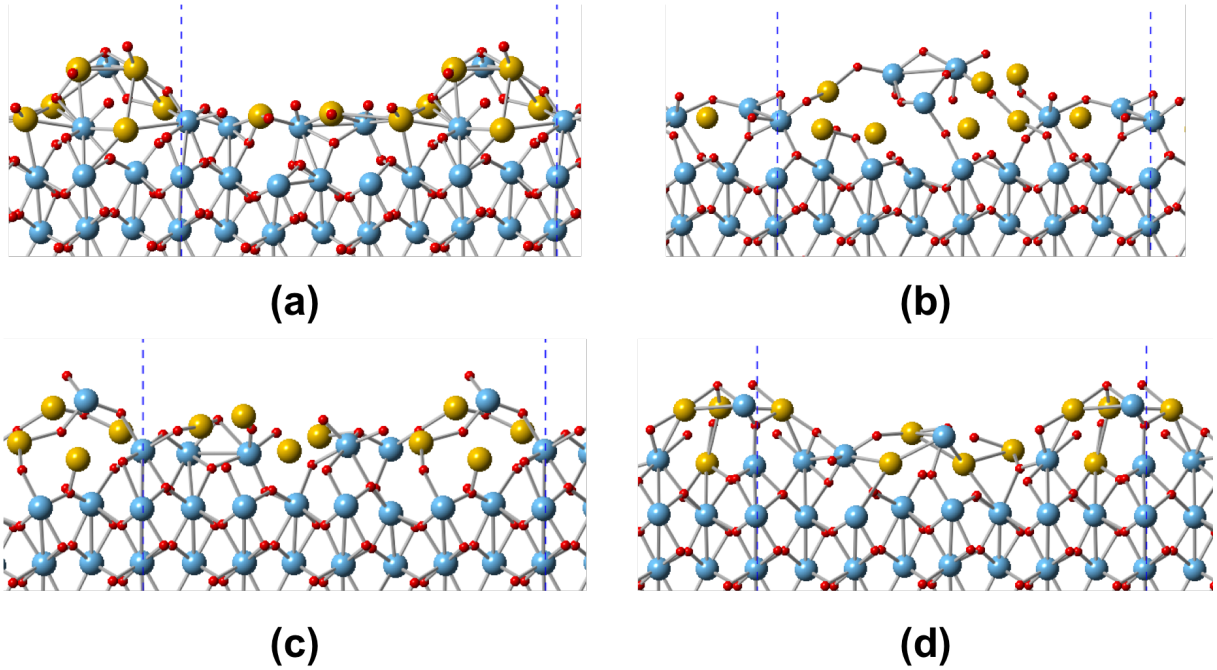

Figure 4: Sideviews of the top layers of the four different structures contributing to the experimental Mg-doped TiO_2(011). Ti atoms are reported in blue, Mg atoms in yellow and O atoms in red. Dashed blue lines stand for the limit of the periodic simulation cell.

Involved processes

The surface structure and composition of a Mg-doped rutile TiO_2(011) crystal are unambiguously determined. We observe the same surface reconstruction as on the pristine crystal. Besides the initial rutile lattice, the surface termination only involves doping Mg atoms in substitutional positions and oxygen vacancies for charge compensation. The presence of excess electrons and interstitial atoms (Mg or Ti) is discarded in the limit of accuracy of our experimental data and confirmed by the calculated structures.

At the surface of the reduced Mg-doped TiO_2(011), Mg segregation brings into play quantities of Mg that go well beyond the defect concentration of less than ten percent[53] since the estimated population of oxygen vacancies created by the Mg segregation amounts to 29% of the oxygen atoms involved in the lattice of the pristine oxide. Formally, this suggests two mechanisms which both lead to the segregation of magnesium and the formation of oxygen vacancies, such that one of these mechanisms totally heals the excess electrons that are present at the reduced oxide surface

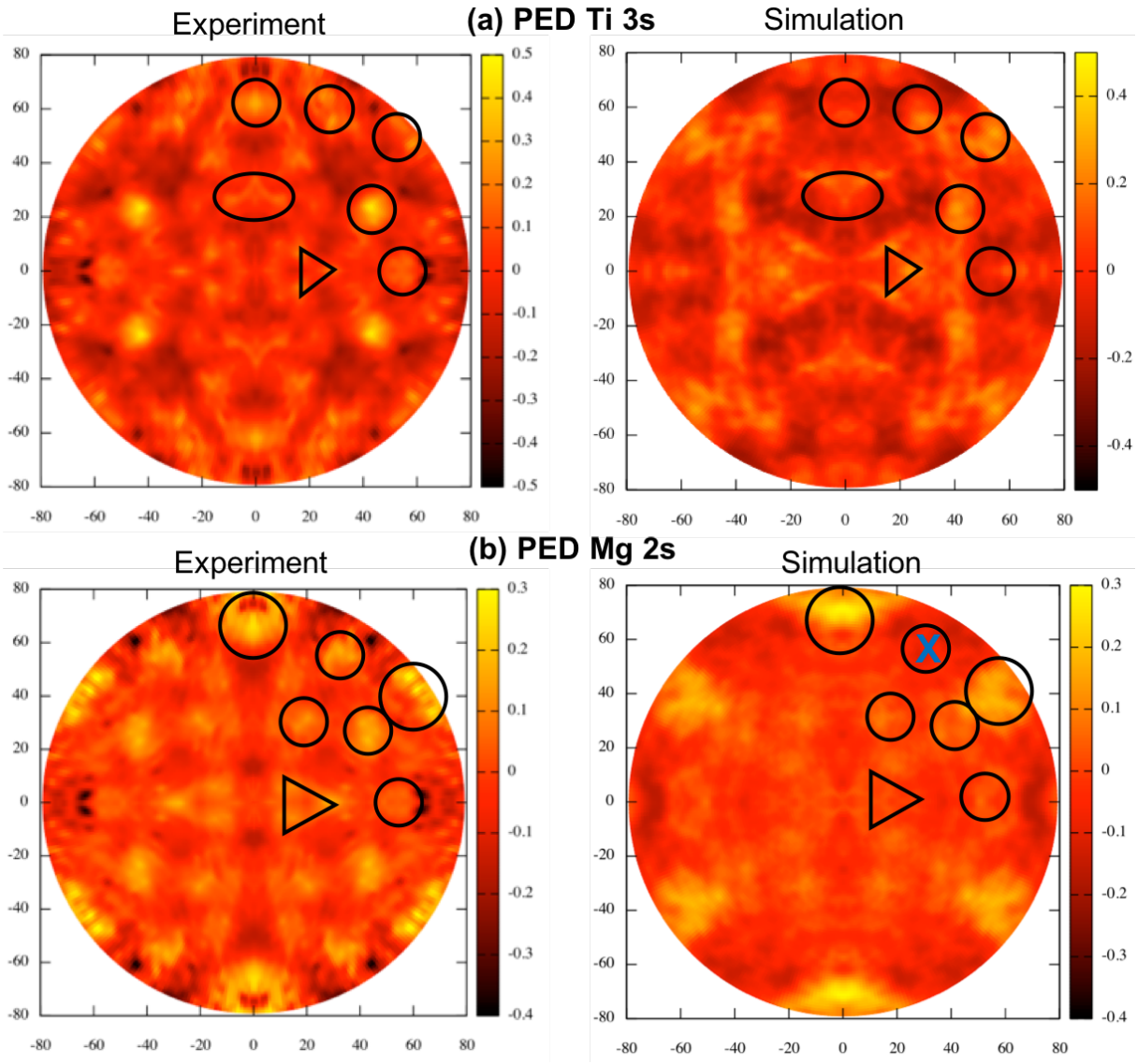

Figure 5: Comparison of the experimental patterns of the (a) Ti 3s (kinetic energy of 455 eV) and (b) Mg 2s (kinetic energy of 428 eV) levels of the Mg-doped TiO_2(011) structure to the simulated patterns obtained by combination of the four configurations reported on Figure 4. In both cases, the main spots of the experimental patterns have been highlighted by circles, ovals and triangles whose sets have been rigidly superimposed to the simulated patterns.

(Figure 2) while the other simply gives rise to oxygen vacancies. That chemistry can be expressed by applying the Kröger and Vink notation[54] to denote charges and lattice sites as well as intrinsic defect formation reactions, involving atoms in lattice sites (O_O and Ti_{Ti}), non-ionized oxygen vacancies ($V_O^{\bullet\bullet}$), titanium ions in interstitial sites ($Ti_i^{\bullet\bullet\bullet\bullet}$) and Mg atoms substituted to Ti in lattice site ($Mg_{Ti}^{''}$). From a simple point of view, the doping reaction by solid MgO ($MgO_{(s)}$) of the stoichiometric TiO_2 can be written, in any part of the material, as:

$$MgO_{(s)} \rightarrow Mg_{Ti}^{''} + O_O + V_O^{\bullet\bullet}(i)$$

This underlines that doping with a metal oxide (i.e. ionic doping) does not generate electron excess while defect charges - substitutional Mg and O vacancies - are balanced. This corresponds to the second of the above-described mechanism. Mg segregation can also be seen to fully scavenge the excess electrons that result from the preparation of the reduced surface by ion bombardment. Indeed, such a treatment gives rise to oxygen vacancies resulting from their preferential sputtering according to:

$$O_O \rightarrow \frac{1}{2}O_{2(g)} + V_O^{\bullet\bullet} + 2e^{'}(ii)$$

leading to excess electrons in superficial layers. During subsequent annealing, a part of the oxygen vacancies may be transformed in interstitial titanium ions with respect to the disappearance of structural units of the crystal according to:

$$2V_O^{\bullet\bullet} + Ti_{Ti} \rightarrow Ti_i^{\bullet\bullet\bullet\bullet}(iii)$$

In non-doped titanium oxide, the reoxidation of surface occurs during annealing through diffusion mechanisms which can involve oxygen ions, oxygen vacancies and/or interstitial titanium ions according to reaction (iv) and/or (v) describing diffusion processes and where superscripts indicate whether the species are in surface or bulk areas:

$$O_O^{bulk} + V_O^{(surf)\bullet\bullet} + 2e^{(surf)'} \rightarrow V_O^{(bulk)\bullet\bullet} + 2e^{(bulk)'} + O_O^{surf} (iv)$$

$$Ti_i^{(surf)\bullet\bullet\bullet\bullet} + 4e^{(surf)'} \rightarrow Ti_i^{(bulk)\bullet\bullet\bullet\bullet} + 4e^{(bulk)'} (v)$$

According to ref[52] about oxygen-induced restructuring of TiO_2(110) surface, subsurface interstitial titanium ions could be the most labile species making the latter process the most likely one. However, MgO doping makes possible a third mechanism. According to reaction (i), such a doping requires to consider oxygen vacancies in addition to Mg atoms substituted to Ti in lattice site. So, to maintain the electroneutrality of the material, in case of Mg ion diffusion, the motion of Mg ions must be accompanied by those of oxygen vacancies. Interdiffusion of magnesium/titanium form bulk/surface to surface/bulk should then be schematized by:

$$Mg_{Ti}^{(bulk)''} + V_O^{(bulk)\bullet\bullet} + Ti_{Ti}^{(surf)} + O_O^{(surf)} \rightarrow Ti_{Ti}^{(bulk)} + O_O^{(bulk)} + Mg_{Ti}^{(surf)''} + V_O^{(surf)\bullet\bullet} (vi)$$

Besides, Mg diffusion can be concomitant to process (iv), leading to the global reaction (vii):

$$O_O^{(bulk)} + V_O^{(bulk)\bullet\bullet} + Mg_{Ti}^{(bulk)''} + Ti_{Ti}^{(surf)} + O_O^{(surf)} + V_O^{(surf)\bullet\bullet} + 2e^{(surf)'} \rightarrow$$

$$O_O^{(bulk)} + V_O^{(bulk)\bullet\bullet} + Ti_{Ti}^{(bulk)} + 2e^{(bulk)'} + Mg_{Ti}^{(surf)''} + O_O^{(surf)} + V_O^{(surf)\bullet\bullet} (viii)$$

which can be summed up as a simple interdiffusion of substitutional Mg and Ti according to process (ix):

$$Mg_{Ti}^{(bulk)''} + Ti_{Ti}^{(surf)} + 2e^{(surf)'} \rightarrow 2e^{(bulk)'} + Ti_{Ti}^{(bulk)} + Mg_{Ti}^{(surf)''} (ix)$$

where motions of neither oxygen ions nor oxygen vacancies are necessary to generate it. Such an interdiffusion phenomenon needs a sufficient magnesium mobility, revealed experimentally without ambiguity by the process of segregation itself, as well as the capacity of titanium ions

to jump from regular sites to interstitial ones (as revealed by ref[52]) in order to allow the magnesium motion. This process shows that during annealing the excess electrons are simply replaced in surface by substitutional magnesium ions without global moving of oxygen ions and/or vacancies. This leaves to a large amount of oxygen vacancies in surface while the excess electrons have fully diffused in the bulk. Considering the amount of Mg detected in surface, reaction (vi) appears to be the dominant mechanism. Writing those reactions according to the Kröger and Vink formalism allows to underline that in absence of a large amount of interstitial titanium ions (revealed by PED patterns), the presence of Mg atoms in the TiO_2 topmost layers as substitutional ions entails the global formation of oxygen vacancies in the surface layers without formation of excess electrons, as experimentally demonstrated by the absence of 3d state in band gap (Figure 2(d)) with the support of DFT calculations.

The DFT approach also demonstrates the stability of the structure and composition of the segregated surface layer. Combined with photodiffraction experiments supported by multiple scattering simulations and measured surface concentrations, DFT determines thermodynamically stable structures of given composition ($Mg_4Ti_3O_{10}$, corresponding to 29% of oxygen vacancies) whose combination corresponds to the surface terminations that are observed. The result is in line with the suggestion by Manzanares et al.[13] of the formation of a surface compound $MgTiO_3$ (25% of oxygen vacancies, a composition close to that found herein) on a Mg-doped TiO_2 photocatalyst active in the reduction of CO_2.

Conclusions

A magnesium segregation has been evidenced by annealing the surface of the reduced Mg-doped rutile TiO_2(011) crystal. Combining photoemission to evaluate the composition of the surface region and resonant photoelectron diffraction to feature the sites occupied by Mg doping elements with DFT simulations to determine the structure of the termination, we arrive at an unambiguous description of the structure and composition of the segregated Mg-rich surface layer, with the

following characteristics:

- segregated Mg ions are substituted to Ti ions in lattice sites; in parallel, oxygen vacancies are associated to segregated Mg for charge compensation while the excess electrons accompany the inward diffusion of Ti ions;
- this reoxidation process allows to completely heal the excess electrons from the surface region after annealing at 870 K as opposed to an undoped surface where such an annealing leaves defect states in the band gap;
- the previously studied surface reconstruction of the pristine $TiO_2(011)$ surface is maintained;
- as determined by DFT, a set of thermodynamically stable structures of given composition represent the Mg-rich surface termination; as a whole, in the surface region, segregated Mg ions appear to have a higher stability than the polaronic distortions that accompany excess electrons.

The segregation mechanism only involves elementary components, titanium, magnesium and oxygen ions, vacancies and excess electrons. It does not require any specific ingredient from the rutile surface that is examined herein, which suggest that similar processes are likely at work for other aliovalent doping elements (with valence < 4) and surfaces of other titania polymorphs.

Acknowledgement

Calculations were performed using HPC resources from DNUM CCUB (Centre de Calcul de l'Université de Bourgogne). The authors also thank the ANR for financial support through project ANR-17-EURE-0002 (EIPHI Graduate School).

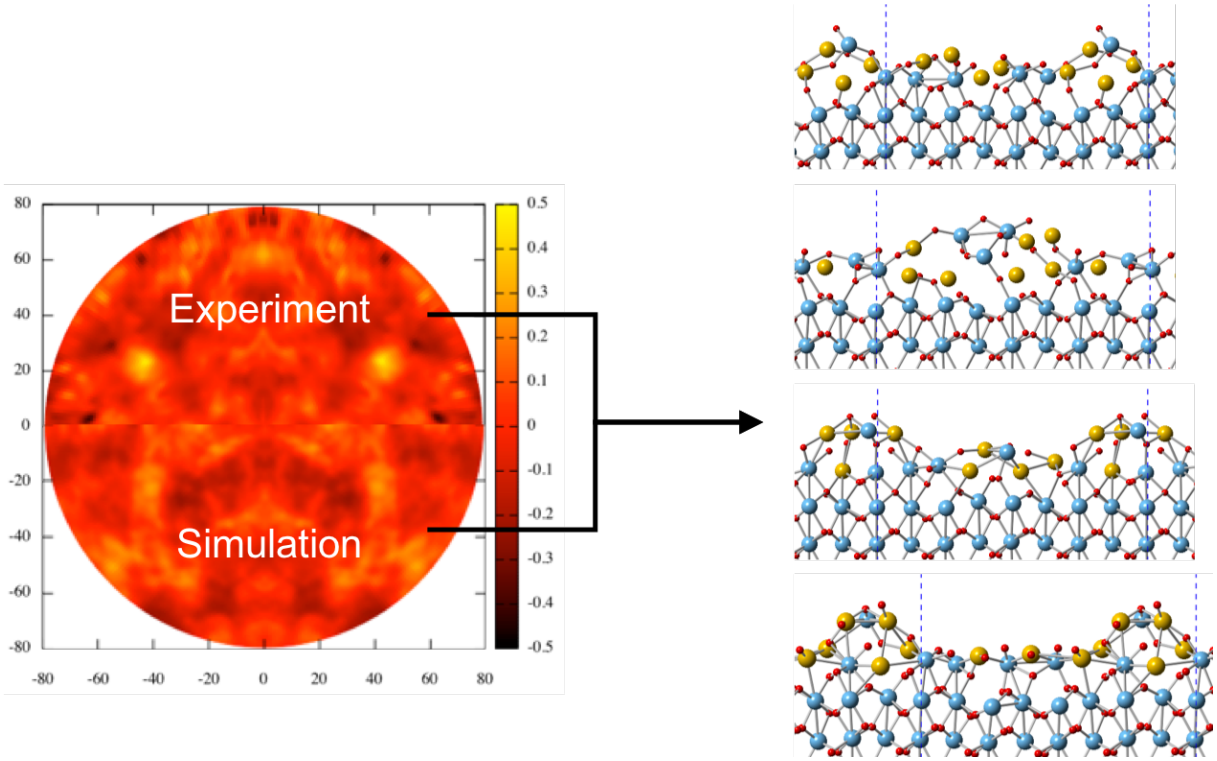

Table of Contents Graphic

References

(1) Chen, X.; Mao, S. S. Titanium Dioxide Nanomaterials: Synthesis, Properties, Modifications, and Applications. *Chem. Rev.* **2007**, *107*, 2891–2959.

(2) Wilke, K.; Breuer, H. Transition Metal Doped Titania: Physical Properties and Photocatalytic Behaviour. *Z. Phys. Chem.* **1999**, *213*, 135–140.

(3) Nowotny, M.; Sheppard, L.; Bak, T.; Nowotny, J. Defect Chemistry of Titanium Dioxide. Application of Defect Engineering in Processing of TiO_2-Based Photocatalysts. *J. Phys. Chem. C* **2008**, *112*, 5275–5300.

(4) Gesenhues, U. Al-doped TiO_2 pigments: influence of doping on the photocatalytic degradation of alkyd resins. *J. Photochem. Photobiol. A* **2001**, *139*, 243–251.

(5) Iwamoto, S.; Sazanami, Y.; Inoue, M.; Inoue, T.; Hoshi, T.; Shigaki, K.; Kaneko, M.; Maenosono, A. Fabrication of Dye-Sensitized Solar Cells with an Open-Circuit Photovoltage of 1V. *Chem. Sus. Chem.* **2008**, *1*, 401–403.

(6) Zhang, C.; Chen, S.; Mo, L.; Huang, Y.; Tian, H.; Hu, L.; Huo, Z.; Dai, S.; Kong, F.; Pan, X. Charge Recombination and Band-Edge Shift in the Dye-Sensitized Mg^{2+}-Doped TiO_2 Solar Cells. *J. Phys. Chem. C* **2011**, *115*, 16418–16424.

(7) Kakiage, K.; Tokutome, T.; Iwamoto, S.; Kyomenac, T.; Hanaya, M. Fabrication of a dye-sensitized solar cell containing a Mg-doped TiO_2 electrode and a Br_3^-/Br^- redox mediator with a high open-circuit photovoltage of 1.21 V. *Chem. Commun.* **2013**, *49*, 179–180.

(8) Liu, Q. Photovoltaic Performance Improvement of Dye-Sensitized Solar Cells Based on Mg-Doped TiO_2 Thin Films. *Electrochim. Acta* **2014**, *129*, 459–462.

(9) Manseki, K.; Ikeya, T.; Tamura, A.; Ban, T.; Sugiuraa, T.; Yoshida, T. Mg-doped TiO_2 nanorods improving open-circuit voltages of ammonium lead halide perovskite solar cells. *RSC Adv.* **2014**, *4*, 9652–9655.

(10) Pathak, S.; Abate, A.; Ruckdeschel, P.; Roose, B.; Gödel, K.; Vaynzof, Y.; Santhala, A.; Watanabe, S.-I.; Hollman, D.; Noel, N.; Sepe, A.; Wiesner, U.; Friend, R.; Snaith, H.; Steiner, U. Performance and Stability Enhancement of Dye-Sensitized and Perovskite Solar Cells by Al Doping of TiO_2. *Adv. Func. Mater.* **2004**, *24*, 6046–6055.

(11) Wang, J.; Qin, M.; Tao, H.; Ke, W.; Chen, Z.; Wan, J.; Qin, P.; Xiong, L.; Lei, H.; Yu, H.; Fang, G. Performance enhancement of perovskite solar cells with Mg-doped TiO_2 compact film as the hole-blocking layer. *App. Phys. Lett.* **2015**, *106*, 121104/1–121104/5.

(12) Koketsu, T.; Ma, J.; Morgan, B. J.; Body, M.; Legein, C.; Dachraoui, W.; Giannini, M.; Demortière, A.; Salanne, M.; Dardoize, F.; Groult, H.; Borkiewicz, O. J.; Chapman, K. W.; Strasser, P.; Dambournet, D. Reversible magnesium and aluminium ions insertion in cation-deficient anatase TiO_2. *Nat. Mat.* **2017**, *16*, 1142–1148.

(13) Manzanares, M.; Fàbrega, C.; Ossó, J.; Vega, L. F.; Andreu, T.; Morante, J. R. Engineering the TiO_2 outermost layers using magnesium for carbon dioxide photoreduction. *App. Catal. B. Env.* **2014**, *150*, 57–62.

(14) Sofianou, M.-V.; Tassi, M.; Boukos, N.; Thanos, S.; Vaimakis, T.; Yu, J.; Trapalis, C. Solvothermal synthesis and photocatalytic performance of Mg^{2+}-doped anatase nanocrystals with exposed {001} facets. *Catal. Tod.* **2014**, *230*, 125–130.

(15) Venkatachalam, N.; Palanichamy, M.; Murugesan, V. Sol-gel preparation and characterization of alkaline earth metal doped nano TiO_2: Efficient photocatalytic degradation of 4-chlorophenol. *J. Mol. Cat. A* **2007**, *273*, 177–185.

(16) Segne, T.; Tirukkovalluri, S.; Challapalli, S. Studies on Characterization and Photocatalytic Activities of Visible Light Sensitive TiO_2 Nano Catalysts Co-doped with Magnesium and Copper. *Int. Res. J. Pure Appl. Chem.* **2011**, *1*, 84–103.

(17) Islam, M.; Bredow, T.; Gerson, A. Electronic properties of oxygen-deficient and aluminum-doped rutile TiO_2 from first principles. *Phys. Rev. B* **2007**, *76*, 045217/1–045217/9.

(18) Shirley, R.; Kraft, M.; Inderwildi, O. Electronic and optical properties of aluminium-doped anatase and rutile TiO_2 from ab initio calculations. *Phys. Rev. B* **2010**, *81*, 075111/1–075111/9.

(19) Shannon, R. Revised effective ionic radii and systematic studies of interatomic distances in halides and chalcogenides. *Acta Cryst. A* **1976**, *32*, 751–767.

(20) Thompson, T.; Yates, J. Surface science studies of the photoactivation of TiO_2-new photochemical processes. *Chem. Rev.* **2006**, *106*, 4428–4453.

(21) Li, J.; Lazzari, R.; Chenot, S.; Jupille, J. Contributions of oxygen vacancies and titanium interstitials to band-gap states of reduced titania. *Phys. Rev. B* **2018**, *97*, 041403/1–041403/5.

(22) Henrich, V.; Dresselhaus, G.; Zeiger, H. Observation of Two-Dimensional Phases Associated with Defect States on the Surface of TiO_2. *Phys. Rev. Lett.* **1976**, *36*, 1335–1339.

(23) Kurtz, R.; Stockbauer, R.; Madey, T.; Roman, E.; de Segovia, J. Synchrotron radiation studies of H_2O adsorption on TiO_2(110). *Surf. Sci.* **1989**, *218*, 178–200.

(24) Zhang, Z.; Jeng, S.; Henrich, V. Cation-ligand hybridisation for stoichiometric and reduced TiO_2(110) surfaces determined by resonant photoemission. *Phys. Rev. B* **1991**, *43*, 12004–12011.

(25) Patel, R.; Guo, Q.; Coks, I.; Williams, E.; Roman, E.; de Segovia, J. The defective nature of the TiO_2(110) (1×2) surface. *J. Vac. Sci. Technol. A* **1997**, *15*, 2553–2556.

(26) Sekiya, T.; Yagisawa, T.; Kamiya, N.; Das Mulmi, D.; Kurita, S.; Murakami, Y.; Kodaira, T. Defects in anatase TiO_2 single crystal controlled by heat treatments. *J. Phys. Soc. Jpn.* **2004**, *73*, 703–710.

(27) Ganduglia-Pirovano, M. V.; Hofmann, A.; Sauer, J. Oxygen vacancies in transition metal and rare earth oxides: Current state of understanding and remaining challenges. *Surf. Sci. Rep.* **2007**, *62*, 219–270.

(28) Saponjic, Z.; Dimitrijevic, N.; Poluektov, O.; Chen, L.; Wasinger, E.; Welp, U.; Tiede, D.; Zuo, X.; Rajh, T. Charge Separation and Surface Reconstruction: A Mn^{2+} Doping Study. *J. Phys. Chem. B* **2006**, *110*, 25441–25450.

(29) Gionco, C.; Livraghi, S.; Maurelli, S.; Giamello, E.; Tosoni, S.; Valentin, C. D.; Pacchioni, G. Al- and Ga-Doped TiO_2, ZrO_2, and HfO_2: The Nature of O 2p Trapped Holes from a Combined Electron Paramagnetic Resonance (EPR) and Density Functional Theory (DFT) Study. *Chem. Mat.* **2015**, *27*, 3936–3945.

(30) Zainullina, V.; Zhukov, V.; Korotin, M. Influence of oxygen nonstoichiometry and doping with 2p-, 3p-, 6p- and 3d-elements on electronic structure, optical properties and photocat-

alytic activity of rutile and anatase: Ab initio approaches. *J. Photochem. Photobiol. C* **2015**, *22*, 58–83.

(31) Krüger, P.; Bourgeois, S.; Domenichini, B.; Magnan, H.; Chandesris, D.; Fèvre, P. L.; Flank, A. M.; Jupille, J.; Floreano, L.; Cossaro, A.; Verdini, A.; Morgante, A. Defect States at the TiO_2(110) Surface Probed by Resonant Photoelectron Diffraction. *Phys. Rev. Lett.* **2008**, *100*, 055501/1–055501/4.

(32) Krüger, P.; Jupille, J.; Bourgeois, S.; Domenichini, B.; Verdini, A.; Floreano, L.; Morgante, A. Intrinsic Nature of the Excess Electron Distribution at the TiO_2(110) Surface. *Phys. Rev. Lett.* **2012**, *108*, 126803/1–126803/4.

(33) Dupont, C.; Bourgeois, S.; Fèvre, P. L.; Verdini, A.; Floreano, L.; Domenichini, B. Structure of TiO_2 (011) revealed by photoelectron diffraction. *Phys. Rev. B* **2016**, *94*, 241304/1–241304/6.

(34) Danger, J.; Fèvre, P. L.; Magnan, H.; Chandesris, D.; Bourgeois, S.; Jupille, J.; Eickhoff, T.; Drube, W. Quadrupolar Transitions Evidenced by Resonant Auger Spectroscopy. *Phys. Rev. Lett.* **2002**, *88*, 243001/1–243001/4.

(35) Le Fèvre, P.; Danger, J.; Magnan, H.; Chandesris, D.; Jupille, J.; Bourgeois, S.; Arrio, M.; Gotter, R.; Verdini, A.; Morgante, A. Stoichiometry-related Auger lineshapes in titanium oxides: Influence of valence-band profile and of Coster-Kronig processes. *Phys. Rev. B* **2004**, *69*, 155421/1–155421/9.

(36) Le Fèvre, P.; Magnan, H.; Chandesris, D.; Jupille, J.; Bourgeois, S.; Drube, W.; Ogasawarag, H.; Uozumih, T.; Kotanihij, A. Interpretation of absorption edges by resonant electronic spectroscopy: experiment and theory. *J. Electron Spectro. Relat. Phenom.* **2004**, *136*, 37–47.

(37) Floreano, L.; Naletto, G.; Cvetko, D.; Gotter, R.; Malvezzi, M.; Marassi, L.; Morgante, A.; Santaniello, A.; Verdini, A.; Tommasini, F.; Tondello, G. Performance of the grating-crystal

monochromator of the ALOISA beamline at the Elettra Synchrotron. *Rev. Sci. Instr.* **1999**, *70*, 3855–3864.

(38) Yeh, J.; Lindau, I. Atomic subshell photoionization cross sections and asymmetry parameters: $1 \leq Z \leq 103$. *At. Data Nucl. Data Tables* **1985**, *32*, 1–155.

(39) Bruno, F.; Floreano, L.; Verdini, A.; Cvetko, D.; Gotter, R.; Morgante, A.; Canepa, M.; Terreni, S. Study of the isotropic contribution to the analysis of photoelectron diffraction experiments at the ALOISA beamline. *J. Electron Spectro. Relat. Phenom.* **2002**, *127*, 85–92.

(40) Oganov, A.; Glass, C. Crystal structure prediction using ab initio evolutionary techniques: Principles and applications. *J. Chem. Phys.* **2006**, *124*, 244704/1–244704/15.

(41) Oganov, A.; Lyakhov, A.; Valle, M. How Evolutionary Crystal Structure Prediction Works-and Why. *Acc. Chem. Res.* **2011**, *44*, 227–237.

(42) Lyakhov, A.; Oganov, A.; Stokes, H.; Zhu, Q. New developments in evolutionary structure prediction algorithm USPEX. *Comput. Phys. Commun.* **2013**, *184*, 1172–1182.

(43) Zhu, Q.; Li, L.; Oganov, A.; Allen, P. Evolutionary method for predicting surface reconstructions with variable stoichiometry. *Phys. Rev. B* **2013**, *87*, 195317/1–195317/8.

(44) Kresse, G.; Hafner, J. Abinitio molecular-dynamics for liquid-metals. *Phys. Rev. B* **1993**, *47*, 558–561.

(45) Kresse, G.; Furthmüller, J. Efficient iterative schemes for ab initio total-energy calculations using a plane-wave basis set. *Phys. Rev. B* **1996**, *54*, 11169–11186.

(46) Perdew, J.; Burke, K.; Ernzerhof, M. Generalized gradient approximation made simple. *Phys. Rev. Lett.* **1996**, *77*, 3865–3868.

(47) Dudarev, S.; Botton, G.; Savrasov, S.; Humphreys, C.; Sutton, A. Electron-energy-loss spectra and the structural stability of nickel oxide: An LSDA+U study. *Phys. Rev. B* **1998**, *57*, 1505–1509.

(48) Pack, J.; Monkhorst, H. Special points for Brillouin-zone integrations"—a reply. *Phys. Rev. B* **1977**, *16*, 1748–1749.

(49) de Abajo, F. J. G.; Van Hove, M. A.; Fadley, C. S. Multiple scattering of electrons in solids and molecules: A cluster-model approach. *Phys. Rev. B* **2001**, *63*, 075404/1–075404/16.

(50) Corneille, J.; He, J.-W.; Goodmann, D. XPS characterization of ultra-thin MgO films on a Mo(100) surface. *Surf. Sci.* **1994**, *306*, 269–278.

(51) Pétigny, S.; Mostéfa-Sba, H.; Domenichini, B.; Lesniewska, E.; Steinbrunn, A.; Bourgeois, S. Superficial defects induced by argon and oxygen bombardments on (110) $Ti0_2$ surfaces. *Surf. Sci.* **1998**, *410*, 250–257.

(52) Henderson, M. A. A surface perspective on self-diffusion in rutile TiO_2. *Surf. Sci.* **1999**, *419*, 174–187.

(53) Yurtsever, A.; Onoda, J.; Abe, M.; Pang, C.; Sugimoto, Y. Imaging the TiO_2(011)-(2$\times$1) Surface using Noncontact Atomic Force Microscopy and Scanning Tunneling Microscopy. *J. Phys. Chem. C* **2016**, *120*, 3390–3395.

(54) Kröger, F.; Vink, H. Relations between the Concentrations of Imperfections in Crystalline Solids. *Solid State Physics* **1956**, *3*, 307–435.